Analysis of local entrainment rate in the initial region of isothermal free swirling jets by Stereo PIV

Fabio Cozzi*, Aldo Coghe, Rohit Sharma

Department of Energy – Politecnico di Milano, Via Lambruschini 4, 20156 Milano, Italy

Entrainment is of crucial importance in many engineering applications, while the relevance of swirling flows is related to their ability to improve mixing in the initial region of a jet, as a consequence of a larger entrainment of ambient air. This is particularly effective at swirl levels above the critical value associated with the onset of vortex breakdown and the generation of the instability referred to as the precessing vortex core (PVC). Despite the importance of the entrainment process in swirling flows, there have been very few quantitative data in the literature. In view of the above observation, the initial region of a swirling gas jet was investigated experimentally using Stereo Particle Image Velocimetry (SPIV) in order to evaluate the local entrainment rate as a function of swirl number and axial distance from the nozzle. The experiments were carried out on a model burner used to generate isothermal swirling air jets at Reynolds number, Re = 21,800. This configuration was chosen due to its relevance to industrial burners and the ability to reproduce a round, turbulent gas jet issuing into ambient air, since this is the most investigated case and allows comparison with previously published results with and without swirl. Measurements were made for the region extending from the nozzle exit to 2.5 nozzle diameters downstream. Several swirl conditions were investigated, characterized by swirl numbers ranging from $S = 0$ to $S = 2.2$. Time-averaged SPIV allowed simultaneous evaluation of the swirl number and characterization of the structure of swirling flows in the near-field region before and after the development of the inner re-circulation zone. The entrainment rate was evaluated by using the integral method applied to the measured SPIV velocity maps. The results provided quantitative evidence that the entrainment rate in the near field is enhanced considerably by the swirl, especially after the onset of vortex breakdown and PVC, reaching values significantly larger than those measured in non-swirling jets. The analysis of the average local entrainment rate revealed a large variability with both the swirl number and the axial distance from the nozzle, leading to the conclusion that the swirl affects the entrainment process in a complex way. The significance of the present results consists in a better understanding of the mixing in the initial region of a typical burner and the possible contribution to validation of numerical modelling of the combustion process.

1. Introduction

Entrainment is an essential feature of shear flows and it is responsible of the observed growth with downstream distance, due to the radial inward flux of ambient fluid. This process controls the mixing rate and is of fundamental interest in the study of fuel injection in many engineering applications, such as scramjet combustors, gas turbine combustors, reciprocating internal combustion engines, and industrial type burners. Effective control of fuel-air mixture is of major concern in reacting cases, since it affects residence time, flame stability, pollutant and soot formation. In recent years, renewed interest focused on the development of efficient schemes for fuel-air mixing, dictated by the need to reduce pollutants and improve performances. Examples are swirling jet flames, where the rapid mixing increases mixture homogeneity and shortens the characteristic time for NOx formation [1–3] or the lean premixing pre-vaporizing (LPP) fuel injection technique in aero-engines [4]. Low NO_x emissions can be achieved also by staged combustion which relies on a first rich premixed zone and a fast secondary air mixing region [5]. These combustion methodologies pose technical and scientific challenges and require accurate analysis of the entrainment process into swirling flows.

The analysis of the initial mixing field of swirling gas jets is of great interest in aero-engine combustors, industrial burners and furnaces as it determines the main features of the combustion dynamics. The relevance of swirling flows relates to their ability to enhance mixing in the initial region of the combustor by increasing the entrainment rate of

---

* Corresponding author.
E-mail addresses: fabio.cozzi@polimi.it (F. Cozzi), aldo.coghe@polimi.it (A. Coghe), rohit.sharma@polimi.it (R. Sharma).

the ambient fluid. They are also characterized by high spreading rate, rapid centreline velocity decay, and high fluctuation levels. Swirling flows are highly three dimensional and unsteady and when the swirl number, as defined in [6,7], exceeds a critical value, the onset of vortex breakdown, associated with the formation of a free stagnation point around the jet axis and a central recirculation zone (CRZ), provides aerodynamic stability to the combustion process and increases the residence time of the reactants in the flame [8]. Strongly swirling flows are also prone to self-excited large scale hydrodynamic instabilities such as the precessing vortex core (PVC) [9–11]. Despite these features have been deeply investigated by many authors up to recent years [7,12–19], poor quantitative information on the entrainment process has been reported, to the authors' knowledge.

Direct experimental investigation of the entrainment mechanism in a jet is difficult since it requires accurate velocity measurements as well as simultaneous detection of the interface between the jet and the surrounding air. Earlier studies used a specially designed porous wall measurement technique for the direct evaluation of the gross amount of entrained fluid into axis-symmetric turbulent free gas jets. With this technique, Ricou and Spalding [20] obtained a simple relationship for the variation of the entrainment rate with axial distance and density ratio valid in the fully developed flow region at large Reynolds numbers. Hill [21] extended the porous wall technique to measure the local entrainment rate in the initial region of turbulent air jets and Delichatsios and Orloff [22] used the same technique to measure air entrainment rates along turbulent buoyant jet flames. This method can only be used under steady conditions and requires a physical structure that intrudes into the flow. Alternative methods based on integration of the velocity profiles or direct entrainment velocity measurements, by Hot Wire Anemometry (HWA) or pressure probes, have been also proposed by different authors [23–27]. The development of laser based techniques, such as laser Doppler Velocimetry (LDV) and Particle Image Velocimetry (PIV), made it possible the direct evaluation of the local entrainment even under unsteady conditions [28], two-phase flows [29–31] or reacting jets [32]. Indeed, the laser techniques are capable of reliable, non-intrusive velocity measurements with directional sensitivity and can provide a more comprehensive picture of the entrainment process.

Two alternative methodologies have been implemented when performing space resolved velocity measurements. Both are finalised to a quantitative assessment of the entrainment rate: (a) integration of the radial profiles of the axial velocity of the jet to evaluate the streamwise increment of the volume flux; (b) direct measurements of the radial velocity component of ambient air entrained into the jet, which provides the radial volume flux. Several experiments have been performed, with both methods, to quantify the entrainment rate of free gaseous non-swirling jets and jet flames [24,32–35]. The first method has some limitations due to errors arising in the numerical integration of turbulent velocity profiles affected by increasing uncertainty in the outer region of the jet, problems in evaluating the variable density in reacting or two-phase flows and possible correlation between density and velocity fluctuations which are usually neglected [22,32]. The second approach assumes the rate of entrainment can be expressed in terms of the radial velocity, since entrained flows are generally directed toward the jet axis. The mean radial velocity (the entrainment velocity) can be measured even for dense sprays or reacting jets, provided the measure is performed sufficiently far from the jet turbulent boundaries, in a region where the density is known and uniform. However, the radial velocity decreases with distance and may become close to the limiting sensitivity of the measuring instrument.

The experimental analysis of the entrainment characteristics of swirling jets poses further challenges. Comparatively few researchers have investigated this problem, and measurement data for strongly swirling flows are still scarce. Earlier and more recent studies [27,36–38] used the integration method to measure the entrainment rate in swirling jets, moreover they all use intrusive techniques such as

the five hole pressure probe [37,38], or the Hot Wire Anemometry [27,36] to measure the flow velocity. The integration method has been also used in confined swirling flames to investigate the recirculation phenomena and entrainment of hot burned gases by LDV [8]. The results obtained by the integration method may become questionable as the swirling strength increases, due to intermittency of the flow, internal recirculation and loss of symmetry. To overcome these difficulties, [39] proposed a different method which is based on Schlieren flow visualization and direct measurement of entrainment velocities in the non-turbulent region around the jet, using Hot Wire Anemometry.

Point-wise measurement techniques, such as HWA or LDV, have the advantage of time resolution at a point in space, but are limited in their ability to provide spatial information at an instant in time. This ability is required when analysing strongly swirling flows with swirl number well above the inception of vortex breakdown and the presence of periodic instabilities. Vortex breakdown (VB) refers to an abrupt change in the flow structure of a vortex, associated with the formation of a steady or unsteady free stagnation point and a central recirculation zone (CRZ) [40]. Above critical swirl number, depending on the swirl generation mechanism and the nozzle geometry, the CRZ may feature a hydrodynamic instability, which corresponds to the regular precession of the large-scale vortical structure around the geometrical axis of symmetry and it is referred to as the precessing vortex core (PVC). Recent advances of quantitative flow visualization techniques such as Particle Image Velocimetry (PIV) made this technique well suited to retrieve detailed information on swirling flows in the VB regime and with a PVC [11,12,16,18,41]. Therefore, PIV seems the most appropriate technique to allow global and instantaneous measurements of the entrainment process. It has been firstly applied to make measurements of the air entrainment velocities into round jets [33], and more recently on a spray plume [31] or a turbulent jet in coflow, by measuring the instantaneous velocity field surrounding the main jet [32]. However, only a few applications to high swirling flows have been reported [42], to the authors' knowledge.

The above observation and the lack of comprehensive studies of swirling jets entrainment as a function of swirl number prompted the current investigation. The Stereo PIV (SPIV) measuring technique has been preferred to analyze the three-dimensional structure of free jets with variable swirl numbers from $S = 0$ to values well above the inception of vortex breakdown. The SPIV is capable of measuring the three components of the velocity and appears the most reliable and accurate since it is less sensitive to out-of-plane motion induced by the high swirl, and it allows simultaneous determination of swirl number and entrainment rate for each operating condition. The entrainment rate was evaluated by using the integral method applied to the mea-sured SPIV velocity maps. The purpose of our investigation was, therefore, the quantitative determination of the influence of swirl number on the entrainment rate in the near field of a free, round gas jet, in the turbulent regime (Re = 21,800), immediately downstream of the nozzle outlet, where the velocity profile develops from that of the en-tering jet to that of fully developed flow.

2. Experimental setup and SPIV system

The experiments were carried out on a vertically mounted model burner schematically shown in Fig. 1 and used to generate isothermal swirling air jets. This configuration was chosen due to its relevance to practical burner geometries, and was already used in previous investigations [5,19]. It consists of a cylinder, 80 mm in diameter and 180 mm in length, followed by a converging section of 160 mm length. At the end of the converging section is located a cylindrical nozzle, with a length of 40 mm and inner diameter D = 36 mm. The nozzle exit is located 7 mm above a 250 mm diameter circular end plate (flange in Fig. 1), characteristic of the original burner design and intended here to prevent generation of large scale disturbances at the nozzle exit [26]. The swirling jet exhausts from the burner nozzle into the quiescent
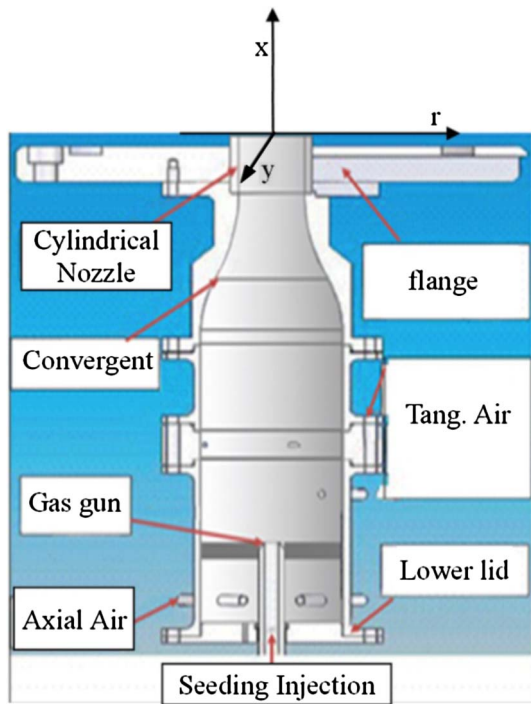
Fig. 1. Sketch of the burner section including the Cartesian reference system x-y-r employed. The origin of the reference system is placed at the center of the exit section of the nozzle, located 7 mm above a 250 mm diameter circular end plate (flange).

ambient air without any co-flow, thus a shear-layer originates between the jet and the ambient air. The nozzle geometry with a retracted plate allows the jet to draw some air from below the nozzle exit plane, favoring an axial velocity component of the entrained ambient air near the nozzle exit. The net result is a positively biased integral estimation of the mass flow rate just at the first axial stations of measurement (see Sections 4 and 4.2). The effect rapidly vanishes at about half diameter downstream the nozzle.

The Cartesian reference system x-y-r attached to the burner is shown in Fig. 1. The origin of the reference system is located at the center of the nozzle exit, the vertical x-axis overlaps the axis of symmetry of the nozzle and the r-axis crosses the nozzle along a diameter. The velocity components along x, y and r respectively are U, W and V. In the measurement plane, i.e. y = 0, W and V correspond also to the tangential and radial velocity components measured in the axial-radial plane of a cylindrical reference system having that plane coincident with the x-r plane.

The swirl generator is of axial-plus-tangential entry type, which allows changing swirl number by varying the axial and tangential flow rates of air. The axial air enters through four radial inlets in the cylindrical chamber and passes through a perforated plate with 24 holes, 2 mm in diameter and 10 mm thick, to produce a uniform axial stream. The tangential air is introduced through eight tangential inlets to impart angular momentum, upstream from the burner throat. The total airflow rate and the swirl number are regulated by controlling flow rates in both the axial and tangential entries through thermal mass-flow meters whose error is estimated ± 1% of reading.

In the present investigation the gas gun of the burner was lowered to about 8D below the nozzle exit section and used to seed the jet with oil droplets produced by a jet atomizer (average diameter 1–2 μm). Previous studies evidenced that the inertial and centrifugal effects on these particles can be considered negligible [13]. To seed the ambient air, oil droplets generated by a six-jet atomizer (average diameter 1–2 μm) were dispersed into the ambient through holes drilled in three vertical pipes located at about 300 mm from the jet axis. Each pipe has a vertical row of holes of 1.5 mm in diameter facing the jet. The two

seeding system are independently regulated to get the proper seeding density in the jet and in its surrounding and achieve accurate Stereo-PIV measurements inside and outside the jet. Care was taken to avoid a possible influence of the surroundings on the free jet. The nozzle outlet is far enough from the surrounding walls, ensuring that the flow may be considered a free swirling jet issuing into the ambient air.

A Stereo-PIV system was employed in order to obtain the instantaneous spatial distribution of the three velocity components in the longitudinal plane of the jet, thus allowing the simultaneous characterization of the swirl number and the streamwise volumetric flux. The field of view was limited to the near field of the jet up to x/D = 2.5 downstream the nozzle outlet, since this region is the most affected by the swirl level in terms of mixing and flow structure. In case of combustion, this is also the region where mixing of reactants and products controls the flame development and stability. Due to laser reflections from the nozzle rim, the PIV measurements were not reliable up to 3 mm above the nozzle exit (x/D $\lesssim$ 0.08), and the velocity vectors were ignored in that region.

The Stereo-PIV system consisted of a double-pulsed Nd:YAG laser operating at λ = 532 nm with a pulse energy of 200 mJ/pulse and a pair of CCD cameras with a resolution of 1344 ∗ 1024 pixels each, equipped with Nikon lenses of 60 mm focal length. The laser sheet was about 1.5 mm thick and passed through a plane lying on the long-itudinal axis of the nozzle. Both cameras, mounted on a traversing system in a Scheimpflug configuration, at opposite sides of the laser sheet, were oriented with an angle of 45˚ to the forward scattering direction. The latter allows to balance the in-plane and out-plane errors in the reconstructed velocity vectors [43].

Double images with an inter frame time of 10–30 μs, depending on swirl number, were acquired at a rate of 5 Hz. The time delay between laser pulses was progressively reduced with the swirl number to avoid out of plane losses of tracer particles. Dantec's Dynamic Studio software was used to acquire and to process the images. The raw images were subjected to an image balancing filter with a smooth cell size of 5 × 5 to correct the non-uniformities of laser light sheet prior to cross-correlation. The background was removed from each PIV image, and an adaptive cross correlation algorithm, including peak validation and 50% overlap area, was implemented. The size of the final interrogation area was 32 × 32 pixels, resulting in a spatial resolution of about 2.5 × 1.7 mm^2. A stereo calibration was performed using a two-level calibration target and the pin-hole camera model. The stereo calibra-tion was corrected for any misalignment between laser sheet and cali-bration target by using the disparity vector map computed from ac-quired SPIV images. The quality of the PIV velocity maps was considered acceptable when less than 5% of the vectors were detected as incorrect.

Finally, the third velocity component was reconstructed from the two 2D vectors fields by using the method proposed by Soloff et al. [44] and implemented in the software. A convergence study, carried out for the mean values of the axial and tangential velocity components, as suggested by [45], proved that 700 PIV snapshots represented an acceptable estimation of the time-averaged velocity field, for all the investigated swirl numbers. As an example in Fig. 2 are shown the computed residuals of the average of U and W for the high swirling jet case (S = 2.2), and at position r/ D≅ 0.42 and x/ D≅ 0.13, where the highest velocity fluctuations are observed and thus slower convergence rate is expected, see Fig. 10e. The residuals show strong oscillations when less than about 50–70 snapshots are used, this is likely a consequence of the high amplitude velocity fluctuations originated by the vortex breakdown and the associated PVC. Increasing the number of snapshots above about 600 makes the residuals of both axial and tangential velocity components less than about 1%.

Errors in the estimation of the amount of ambient air entrained into the jet arise from the PIV measurement global error, the possible lack of symmetry of the flow at increasing swirl, the very low velocities near the jet boundary and the uncertainty of the axial position. By
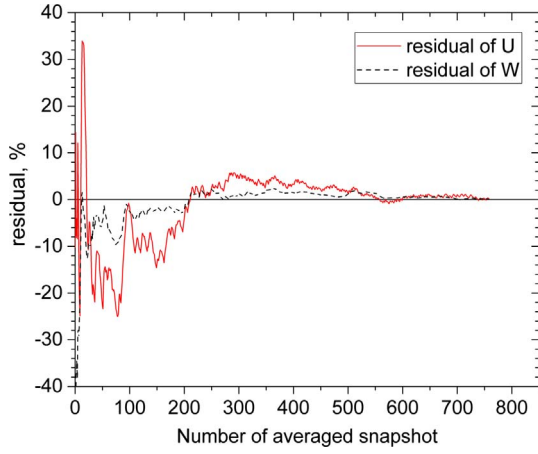
Fig. 2. Convergence of mean axial and tangential velocities with increasing SPIV snapshots at $r/D \cong 0.42$ and $x/D \cong 0.13$ and $S = 2.2$.

optimizing the quality of images, seeding particle density and uniformity, time between frames, validation criteria and the size of the interrogation window, it is estimated that in the reported experiments the largest uncertainty in the mean velocities are mainly ascribed to the statistical error. A sample of an instantaneous SPIV map is shown in Fig. 3 to highlight the overall good quality of the measurements, since no further validation or smoothing have been applied to the instantaneous maps besides those embedded in the adaptive cross correlation algorithm.

The jet was heavily seeded so that there were at least 10 particles in each interrogation window and each imaged particle was about 2 pixels in diameter. Under those conditions and using the evaluation strategy previously described, the random uncertainty of the correlation peak-finding algorithm can be estimated to be about ± 0.1 pixels [46,47]. Since both cameras contribute symmetrically to the measurement, the in-plane error is smaller by a factor $1/\sqrt{2}$ than the value for the single camera arrangement and the error of the out-of-plane component equals the in-plane error multiplied by $1/\tan(\phi)$ [43], where ϕ is the angle between the light sheet normal and the camera viewing direction ($\phi = 45°$ in our case).

The statistical error is affected by the velocity fluctuations existing within the swirling jet. By assuming a $(1-\alpha)\%$ confidence interval, the relative error of the mean axial velocity component, $\varepsilon_{\overline{U}}$, is computed as:

$$\varepsilon_{\overline{U}} = \frac{Z_{\alpha/2}}{\sqrt{N}} \frac{u'}{\overline{U}_{bulk}} \tag{1}$$

where $Z_{\alpha/2}$ is the confidence coefficient in the $(1-\alpha)\%$ confidence interval, $Z_{\alpha/2} = 1.96$ when $(1-\alpha)\% = 95\%$, N is the sample size if independent samples, u' is the r.m.s. fluctuation of U and $\overline{U}_{bulk}$ is the bulk velocity defined as the volumetric air flowrate divided by the nozzle area $\pi D^2/4$. In the present case $\overline{U}_{bulk} = 8.9$ m/s.

The instantaneous velocity maps can all be considered as statistically independent samples, being the sampling time of the SPIV system, $T_{SPIV} = 0.2$ s, much larger than two times the integral time scale, T_i. Where the latter is estimated following Martinelli et al. [13] from the convective time scale: $T_i = D/\overline{U}_{bulk} \cong 0.004$ s.

In the present case, the relative error $\varepsilon_{\overline{U}}$ of the calculated mean values is limited to ± 4% of bulk velocity, with a sample size N = 700 image pairs, and $u'/\overline{U}_{bulk} = 50\%$. The latter value is representative of the maximum r.m.s. velocity fluctuations for all the tested cases, except a few points for the axial velocity component close to the nozzle exit, see Fig. 10. Being the analysis focused on the entrainment evaluated through the mean velocity field, the sample size is appropriate to achieve a satisfactory first order statistics.

3. Theoretical considerations and experimental methodology

From the full-field instantaneous velocity maps provided by the SPIV technique for each image pair, the local components of jet velocity are resolved and the mean structure, considered representative of the investigated isothermal steady jet, is evaluated by ensemble averaging the 700 instantaneous frames. For an axisymmetric gas jet, the entrained mass flow rate, $\dot{m}_e(x)$, up to the generic axial location, x, can be computed by integrating the corresponding mean axial velocity profile, $\overline{U}(x,r)$:

$$\dot{m}_e(x) = 2\pi\rho \int_0^{R_j} \overline{U}(x,r)r\,dr - \dot{m}_0 \tag{2}$$

where R_j is the radius of the jet, defined as the minimum radial distance where the axial velocity vanishes, and $\dot{m}_0$ is the mass flow rate at the jet exit (i.e. x = 0).

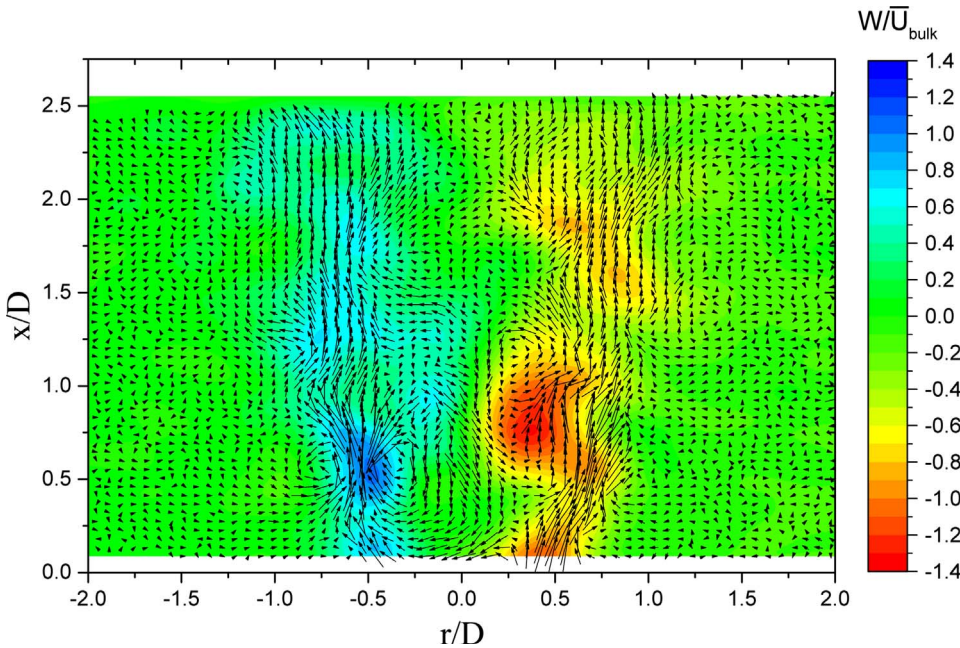The local entrainment rate, En, is then estimated by evaluating the

Fig. 3. Exemplary of a single instantaneous SPIV map for the $S = 2.2$ case, vectors show the in-plane instantaneous velocity components (U and V), while the color map shows the instantaneous out-of plane velocity W. All velocity components are normalized with $\overline{U}_{bulk}$.

Re	S_g	S	$\overline{W}_{max}/\overline{U}_{bulk}$	$\overline{W}_{max}/\overline{U}_{max}$	VB	PVC
21,800	0.0	0.0	0.00	0.00	No	No
	1.15	0.45	0.65	0.61	No	No
	1.8	0.78	1.01	0.95	No	No
	2.6	1.1	1.01	0.95	Yes	No
	4.6	1.4	1.10	1.03	Yes	Yes
	7.2	2.2	1.12	1.05	Yes	Yes

rate of change of mass flow rate $\dot{m}(x) = \dot{m}_e(x) + \dot{m}_0$ [48,49], which is equal to the rate of change of the entrained mass flow rate:

$$En = \frac{d\dot{m}}{dx} = \frac{d\dot{m}_e}{dx} \tag{3}$$

Introducing the nozzle diameter D and the mass flow rate at the jet exit, $\dot{m}_0$, a non-dimensional local entrainment rate may be defined [21,30,39]:

$$K_{el} = \frac{D}{\dot{m}_0}\frac{d\dot{m}_e}{dx} = \frac{D}{\dot{m}_0}En \tag{4}$$

which is not necessarily a constant in the initial region, before the jet reaches the fully developed state.

Additionally, under steady conditions, a non-dimensional entrainment coefficient, K_e, can be expressed in terms of the ratio of the entrained mass flow rate into the jet, at a generic distance x from the nozzle, $\dot{m}_e(x)$, and the mass flow rate at the jet exit, $\dot{m}_0$:

$$\frac{\dot{m}_e(x)}{\dot{m}_0} = \frac{\dot{m}(x)-\dot{m}_0}{\dot{m}_0} = K_e\frac{x}{D} \tag{5}$$

In the present experiment the jet has the same constant density of the ambient gas, i.e. air, thus in Eq. (5) the density ratio between the two gases is omitted. In fully developed axisymmetric non swirling jets K_e is a constant equal to $\cong 0.32$ [20], while in the near field region K_e results to be a function of the distance from the nozzle [21,32].

Following [26,39] we preferred to define a non-dimensional entrainment rate, $\Psi(x)$, which will be used to report the present experimental results:

$$\Psi(x) = \frac{\dot{m}_e(x)}{\dot{m}_0} = \frac{\dot{m}(x)}{\dot{m}_0}-1 \tag{6}$$

A relationship between K_e and K_{el} can be easily found by integrating Eq. (4) between the nozzle exit, $x = 0$ and the generic downstream position x_{end} and comparing with Eq. (5):

$$K_e = \frac{1}{x_{end}}\int_0^{x_{end}} K_{el}dx \tag{7}$$

According to Eq. (7), K_e is the average value of K_{el} over the interval $0 \leq x \leq x_{end}$. On the other hand K_{el} results also to be the derivative of $\Psi(x)$ with respect to x/D, see Eq. (8).

$$K_{el} = \frac{D}{\dot{m}_0}\frac{d\dot{m}_e}{dx} = \frac{d\Psi(x/D)}{d(x/D)} \tag{8}$$

The characteristics of a swirling jet are usually represented by the Reynolds number, Re, based on the bulk volumetric flow rate and the nozzle throat diameter, and the swirl number, S, which is commonly based on the ratio of axial flux of angular momentum to the axial flux of axial momentum multiplied by the nozzle radius [6]. This swirl number definition is usually simplified, assuming boundary-layer approximations and negligibly small turbulent stresses with respect to the mean velocity terms [7,38], and reduces to:

$$S = \frac{\int_0^R r^2\overline{UW}dr}{\left[\int_0^R r\left(\overline{U}^2-\frac{1}{2}\overline{W}^2\right)dr\right]*R} \tag{9}$$

where $\overline{U}$ and $\overline{W}$ are the time averaged axial and azimuthal velocity components and $R = D/2$ is the radius of the nozzle. This definition provides an integral property of the swirling jet and relies only on the measured mean velocity profiles, eliminating the need to measure static pressure and allowing to be easily implemented by using stereo PIV. The inherent complication in the practical use of Eq. (9) with different measuring techniques has led many authors to develop analytical expressions, which are hardly comparable when applied to different flows, since it has been demonstrated that the swirl generating me-chanism influences the initial velocity profiles [7]. It is also known that estimates of S from analytical expressions differ from values deduced from experiments. However, an accurate and repeatable knowledge of the swirl number was a prerequisite to the present investigation and, in addition to the above mentioned swirl number, it was found that another convenient way to monitor S, during each section of the PIV measurements, was to use a geometrical swirl number S_g defined as [50]:

$$S_g = \frac{\pi r_0 R}{2A_T}\left(\frac{\dot{m}_T}{\dot{m}_T + \dot{m}_A}\right)^2 \tag{10}$$

where A_T is the total area of the eight tangential air inlets, r_0 is the radius of the air tube where the tangential air is injected. Eq. (10) al-lows to monitor S simply by monitoring the mass flow rates of the axial air, $\dot{m}_A$, and tangential air, $\dot{m}_T$. For the present investigation, the ana-lytical expression of S_g has been indicated together with estimates of S from Eq. (9) based on the mean axial and tangential velocity profiles measured by SPIV at the jet outlet for each operating condition (see Table 1). In the Table 1 are also reported the ratios of the maximum tangential to axial velocities and the indication of the presence of vortex breakdown and PVC, as will be discussed later.

The experiments were performed at a fixed Reynolds number of 21,800 based on nozzle diameter, the bulk mean velocity, $\overline{U}_{bulk}$, and the dynamic air viscosity, μ. Several swirl conditions were investigated, characterized by swirl numbers ranging from $S = 0$ to $S = 2.2$ (see Table 1). Column VB in Table 1 also shows if the vortex breakdown occurred at the specified S, the breakdown state being identified by the first occurrence of a time averaged axial velocity ≤ 0 on the burner axis. In the present experiment, the vortex breakdown occurs at $x/D = 0.84$, for $S = 1.1$, as it will be shown in Figs. 5 and 6(d). As observed in a previous work on the same set-up and with same operational conditions [19], the occurrence of the Precessing Vortex Core (PVC) instability, shown in Table 1, is identified by a clear peak in the spectral analysis of the pressure fluctuations measured by a capacitive micro-phone. As an example a few power spectral densities of pressure fluctuations for the swirling and non-swirling cases are shown in Fig. 4 as a function of the Strouhal number $S_t = fD/\overline{U}_{bulk}$, where f is the frequency, see [19] for details.

Firstly, the non-swirling case has been investigated to verify the accuracy of the experimental procedures adopted. The results are compared with literature data referred to the initial region of a free jet. The effect of swirl number is then analysed, from moderate to high swirl, through the critical region where the PVC instability arises. Comparison with entrainment data obtained by Park and Shin [39] with a different measuring technique and under similar flow conditions, is also reported.

4. Experimental results

4.1. Time averaged flow field

To evidence the changes in the jet structures originated by increasing the swirl number, the time averaged velocity maps measured in the central plane of the jet for different swirl levels are shown in Fig. 5. Velocities are scaled with respect to the bulk velocity of the jet, U_{bulk}, and the spatial coordinates have been normalized by the burner
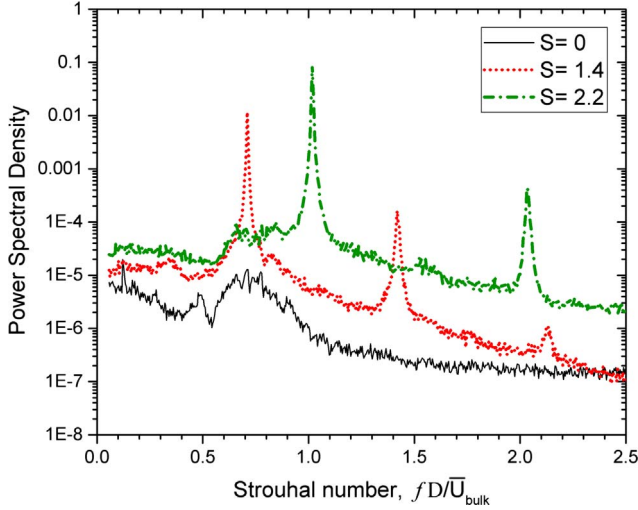
Fig. 4. Power spectral density of microphone signals for the non-swirling and swirling jets as a function of Strouhal number $= fD/\overline{U}_{bulk}$. The first sharp peak visible at both $S = 1.4$ and $S = 2.2$ is the fundamental frequency of PVC while peaks at higher Strouhal number are higher harmonics.

nozzle diameter $D = 36$ mm. For clarity the axial and radial velocity components, i.e. $\overline{U}/\overline{U}_{bulk}$ and $\overline{V}/\overline{U}_{bulk}$, are shown as a vector and only one every four radial profiles is reported in each map. The color maps show the tangential velocity $\overline{W}/\overline{U}_{bulk}$. In the pre-breakdown regime, Fig. 5(a, b and c), the width of the jet gradually increases in the downstream direction and the jet divergence also increases by increasing the swirl number. Despite at $S = 0.78$ a clear deficit in the axial velocity profiles is observed close to the jet axis, a reverse/stagnation axial flow is never detected in the time averaged maps for this regime. On the other side, in the breakdown/post-breakdown regimes, Fig. 5(d, e and f), the jet spreads out quickly in the very near field, $x/D \lesssim 1$, and a central reverse/stagnation axial flow appears, while downstream the jet width grows more slowly. To better highlight jet evolution in the downstream direction, the radial profiles of the normalized axial and tangential velocity components extracted from the ensemble averaged PIV maps are also shown in Figs. 6 and 9.

For $S = 0$, the velocity profile at the efflux section has the characteristic features of a turbulent jet flow, and evidences the existence of a perfectly axisymmetric jet flow field. At very close distance from nozzle exit, $x/D \cong 0.13$ in Fig. 6(a), the radial extension of the positive axial velocity is larger than the nozzle diameter, indicating the presence of an additional axial velocity component of the flow drawn alongside the nozzle tube between the end-plate surface and the nozzle exit. The latter gives rise to a higher measured flow rate very close to the nozzle exit with respect to the imposed flow rate. At moderate swirl numbers, the velocity distribution modifies considerably, and is characterized by an increasing lack of symmetry. Close to the nozzle exit, the jet shows a strong bimodal axial velocity profile. Moving downstream the increasing jet width and mixing with the still ambient air smooth out the radial velocity profiles, at the same time they favour a decrease of the axial velocity in the core region until the inner recirculation zone appears, related to the onset of the vortex breakdown (VB) phenomenon. For the investigated jet, the critical value is observed for swirl numbers around ($S = 1.1$, $S_g = 2.6$), very close to the results reported by [7,11] and attributed to the way the swirl is generated in the nozzle. The critical value has been associated with the first appearance of flow stagnation/reversal as shown in Fig. 6(d). The shape of the reverse flow region is shown in Fig. 7 for $S \geq 1.1$ by the isoline of zero axial velocity. The recirculation zone increases in length and width by increasing the swirl number and at $S = 2.2$ its length extends to within the nozzle and downstream to about $x/D \sim 2.5$, while its maximum non-dimensional width, Δ_{CRZ}/D, reaches a value of about 0.66. At swirl number higher

than the critical value the insurgence of a periodic motion (PVC) was observed and its characteristic frequency measured by a microphone (see Fig. 4) [19]. The velocity defect on the axis induces a sensible asymmetry in the axial velocity distributions at moderate swirl, while at higher swirl ($S \geq 1.1$, $S_g \geq 2.6$) once the onset of VB has occurred, the axial velocity distribution recovers an almost axisymmetric shape.

Asymmetries in the flow field of both high and low swirl jets have been observed by other authors. For the high swirl case they show up in the instantaneous velocity maps as a consequence of vortex breakdown and PVC phenomena [10,12,52,53]. At low swirl the time-mean velocity map can show a non-axisymmetric structure, which is usually attributed to the high sensitivity of the flow to small asymmetries in the system geometry [53]. Sometimes the asymmetry is quite small and observed at both high and low swirl levels, see for example Fig. 3 of [18] and Fig. 10 of [51] where the authors provide no comments on that. In our case, great care was put in assembling all the burner components, anyhow the observed asymmetry at moderate swirl, cases $S = 0.45$ and $S = 0.78$ in Fig. 5(b) and 5(c), could be originated by imperfections of the burner geometry or slight unevenness of the flow at the tangential injection section. However, this hypothesis seems to be contradicted by the symmetric velocity profiles observed without swirl and after the inception of the vortex breakdown. Careful examination of the instantaneous axial velocity maps reveals that such asymmetry is linked to an asymmetric and random in time appearance in the jet of axial velocities less than or equal to zero (i.e. stagnation/counter flow). This phenomenon could be related to an intermittent reverse flow whose strength and probability of occurrence are small enough to not be detectable in the time mean velocity maps. The intermittency of the VB at low swirl level has already been observed by Oberleithner et al.[11] and Markovich et al. [18], anyhow they did not mention those asymmetries in their reports. To analyze the flow asymmetry observed in the present work the probability that the instantaneous axial velocity $U_i(r/D, x/D) \leq 0$ is evaluated as:

$$p(r/D, x/D) = \frac{\sum_{i=1}^{N} \{U_i(r/D, \ x/D) \leqslant 0\}}{N} \tag{11}$$

where i is the generic snapshot, N is the total number of snapshots and the quantity $\{U_i(r/D, x/D) \leqslant 0\}$ can have two values: 1 if true, 0 otherwise. The function $p(r/D, x/D)$ can be thought to represent the fraction of time of a unitary time interval, during which the stagnation/ reverse axial flow shows up at location $(r/D, x/D)$. Thus if in every snapshot $U_i(r/D, x/D) \leqslant 0$ the summation in Eq. (11) results to be equal to N and we get $p(r/D, x/D) = 1$, while at locations where the axial velocity is never ≤ 0 the summation is nil and $p(r/D, x/D) = 0$.

Fig. 8 shows the time-mean vector fields (vectors represent the in-plane velocity components) for the $S = 0.45$ and $S = 0.78$ cases. On the same figure the iso-lines of equal probability are superimposed along with the percentage value of p. Fig. 8 clearly evidences that $p(r/D, x/D)$, besides assuming values greater than zero, has an asymmetric shape that correlates with the one shown by the time mean velocity maps, i.e. is the side of the jet showing higher value of $p(r/D, x/D)$ to show a deficit in the time mean axial velocity. Thus the asymmetric and intermittent occurrence of a reverse flow shows up as an asymmetric mean flow field. To minimize its effect on the entrainment analysis, the jet mass flow is estimated over the full jet diameter instead of using just one half of the axial velocity profile, see Section 4.2.

By contrast, the tangential velocity profiles show an antisymmetric structure for any swirl number, and typical examples are shown in Fig. 9. Due to the conservation of angular momentum, the maximum of the tangential velocity decreases with distance from the nozzle.

Indicative examples of the radial distributions of the r.m.s. fluctuations of the axial and tangential velocities normalized by the bulk velocity, $u'/\overline{U}_{bulk}$ and $w'/\overline{U}_{bulk}$ respectively, are reported in Fig. 10. In absence of swirl, the intensity of the r.m.s. fluctuations increases with
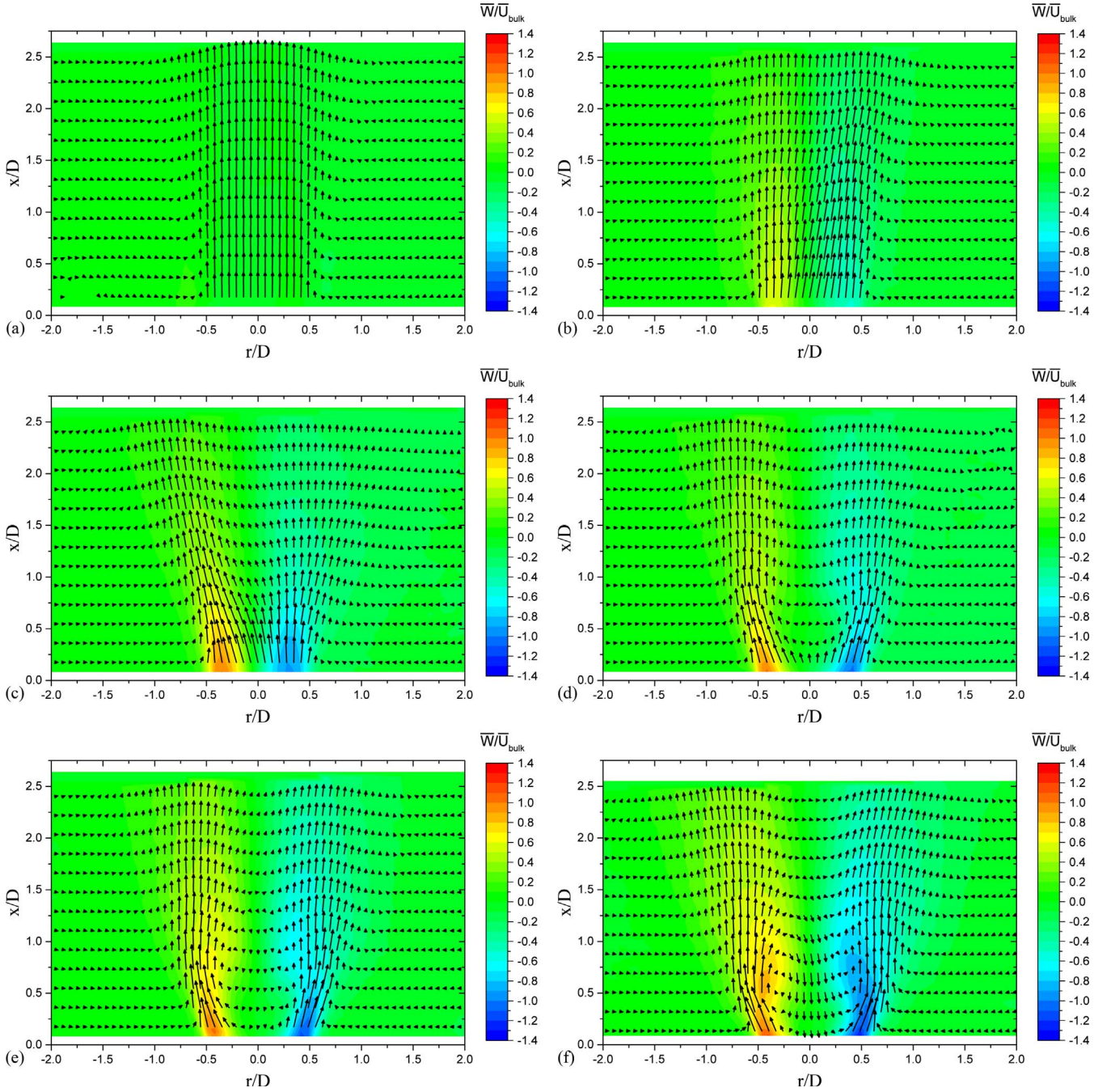
Fig. 5. Time averaged flow field for the (a) $S = 0$, (b) $S = 0.45$, (c) $S = 0.78$, (d) $S = 1.1$, (e) $S = 1.4$ and (f) $S = 2.2$ cases. Vectors show in-plane velocities $\overline{U}/\overline{U}_{bulk}$ and $\overline{V}/\overline{U}_{bulk}$, the color maps show the out of plane component $\overline{W}/\overline{U}_{bulk}$.

distance from the nozzle for the axial component and it does the opposite for the tangential, reaching similar levels at x/ D⩾ 2, although fully isotropy is never reached in the investigated region. A tendency of the velocity fluctuations to become more anisotropic with increasing swirl is also suggested by Fig. 10(c–f). At the onset of vortex breakdown ($S = 1.1$), we observe higher values of the velocity fluctuations for the axial component, compared to the tangential one. This behaviour seems associated with increasing instability of the stagnation point in the near field of the nozzle. After vortex breakdown, the velocity fluctuations become very large in the inner shear layer between the central recirculation region and the jet main stream, indicating the intense mixing favoured by the large scale vortical structures originated by the high swirl. At $S = 2.2$, the radial profile of the r.m.s. of the tangential velocity fluctuations is different from the axial one, compare Fig. 10(e–f),

being characterized by an additional central peak related to the well known phenomenon of the precession of the vortex core (PVC) [13,16,54].

All Reynolds shear stresses, normalized by $\overline{U}_{bulk}^2$, are nearly zero for the non-swirling case and increase when the swirl number is increased, and their profiles broaden in the near field region extending up to x/ D ~ 1, where their highest values were found.

All three normalized Reynolds shear stresses, the axial–radial $u'v'/\overline{U}_{bulk}^2$, the radial–azimuthal $v'w'/\overline{U}_{bulk}^2$, and the axial–azimuthal $u'w'/\overline{U}_{bulk}^2$, result to be much smaller than the Reynolds normal stresses with the peak value of $u'w'/\overline{U}_{bulk}^2$~40% that of $(u'/\overline{U}_{bulk})^2$ for the maximum swirl number.
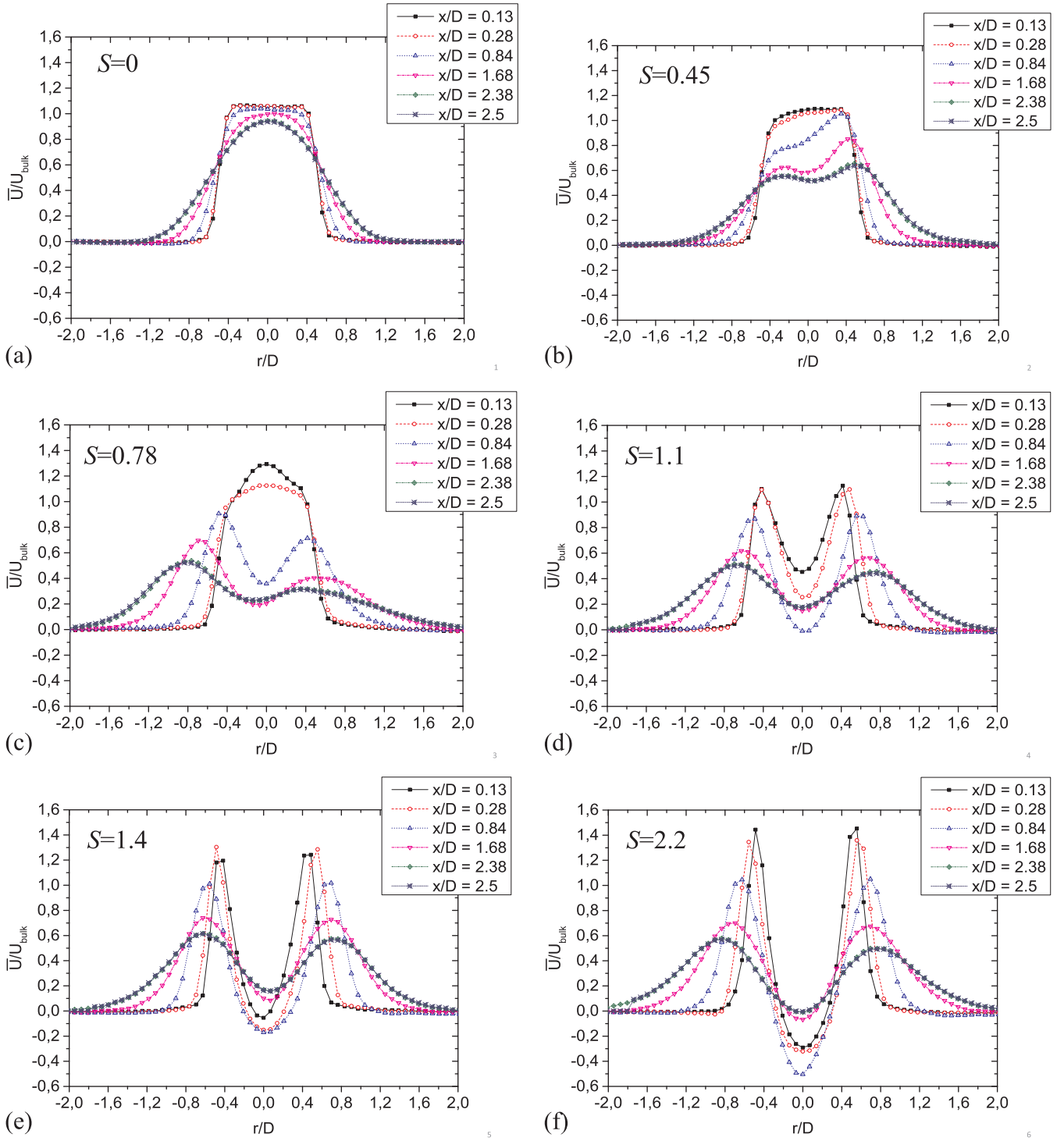
Fig. 6. Radial profiles of the time averaged axial velocity component at increasing axial distance from the nozzle for different swirl numbers S.

4.2. Air entrainment

In the present investigation the mass flow rate of the jet at each axial location, $\dot{m}(x)$, is evaluated by integrating the mean axial velocity profile along the radius up to a radial distance, $R_{j\pm}$, where $|\overline{U}(x,R_{j\pm})| \leqslant 0.1$ m/s. To minimize the impact of non-perfect symmetric axial velocity profiles on the estimation of both $\dot{m}(x)$ and $\dot{m}_e(x)$, the integral in Eq. (2) is actually carried out between R_{j-} and R_{j+} as shown in Eq. (12).

$$\dot{m}_e(x) = \pi\rho \int_{R_{j-}}^{R_{j+}} \overline{U}(x,r)r\,dr - \dot{m}_0 \tag{12}$$

Based on the uncertainty of mean velocities, the statistical error of the volumetric flow rate is estimated to be less than $\pm$ 4%.

Close to the nozzle exit ($x/D \cong 0.1$) the mass flow rate evaluated for the non-swirling jet ($S = 0$) was found larger than the one measured by the thermal mass flow meters, $\dot{m}_0$, the difference being above the experimental errors and of the order of 10%. As already introduced in Sections 2 and 4, this result is attributed to the recessed end plate that induces an entrained air flow having a non-zero axial velocity
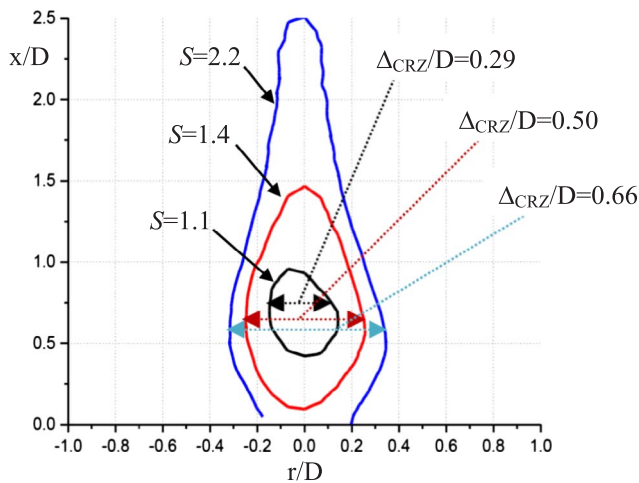
Fig. 7. Shape of the recirculation zone defined by the iso-line of zero axial velocity for different swirl numbers S. Its non-dimensional maximum width, Δ_{CRZ}/D, is also shown.

component. Thus very close to $x/D = 0$, Eq. (12) estimates an higher flow rate as compared to the one measured by mass flow meters. The effect disappears at about 0.5D from the nozzle exit, see Fig. 11. At higher swirl numbers, larger differences were measured which are justified by a progressive increase of the entrainment of ambient air in the very near zone of the jet, as revealed by the present results.

4.2.1. Non-swirling jet

The non-swirling free jet case has been investigated to establish the accuracy of the measurement procedure and the reliability of the experimental apparatus. The experiments have been performed at a Reynolds number, Re = 21,800, sufficiently high to favour the development of a free turbulent jet and to allow comparison with previous investigations [21,24,26,39].

The non-swirling data are reported (Fig. 11) in the form of normalized entrainment rate, Ψ, vs axial distance from the jet outlet, normalized to the nozzle diameter, x/D. The present data are very close to those reported by Trabold at al. for a similar nozzle geometry (L/D ~ 1) and Reynolds number [26]. They differ only in the initial region since we have a retracted end plate, while [26] had a flanged section at the nozzle exit. It must be noted that [26] used the same integration method, although the measurements were made by a Pitot probe.

To the authors' best knowledge, in such very near region of the jet, i.e. $0 \leq x/D \leq 1$, there are no available published measurements to compare with our results. Assuming that an initial bias is present in our

mass flow rate measurements, the rate of increase of the entrainment is reasonably lower in the initial region extending up to $x/D = 0.5$, and then it varies almost linearly with the downstream distance, as found by other authors in the initial region downstream the nozzle exit.

Present entrainment values are sensibly higher than Hill's data, while the results of [24,39], both obtained by using Hot Wire Anemometry, are a bit lower, although they were obtained at Re numbers different than our (Re = 20,500, and Re > 50,000 in [24,39], respectively). However, the comparison is not fully appropriate since the various experimental setups were not exactly the same, in terms of nozzle geometry and inlet conditions, and also the measurement methods were substantially different. It must be noted that, as suggested by [26], in the initial region the entrainment rate is very sensitive to the geometry of the nozzle, resulting lower for a convergent nozzle than for a sharp-edged one. The above results and observations corroborate the validity of the present measurement method and experimental setup.

4.2.2. Swirling jet

The effect of swirl on the non-dimensional entrainment rate is illustrated in Fig. 12(a). Results indicate that entrainment rate in the near field is significantly larger for swirling jets compared to the non-swirling case. As the swirl number approaches the breakdown regime the results show an abrupt increase of the entrainment rate followed by a further more regular increase with S, at least in the investigated range. However, in the critical regime ($0.78 \leq S \leq 1.1$) the entrainment curves show a reversed order compared to the general trend, with higher entrainment at lower swirl, although the two curves are very close in most of the investigated range. This behaviour could be as-cribed to both the unsteady conditions of the jet and its non-symmetric axial velocity profiles (see Figs. 5 and 6). It must be noted that these conditions alter significantly the symmetry of velocity profiles, which is implicitly required when using the integration method and may reduce the accuracy of the numerical integration, providing less reliable re-sults. The onset of vortex breakdown is clearly a transition period in the jet development with profound effects on the shear layers and the mixing with ambient air.

The entrainment rates in Fig. 12(a) show a more or less linear trend with axial distance and a tendency toward an asymptotic behaviour appears at the highest swirl number. It may be reasonable that far downstream the entrainment rate stabilizes, although further measurements at larger axial distances are necessary to confirm the observation. To a further analysis, it can be observed that the $S = 1.1$ case presents an entrainment rate that grows almost linearly with the axial distance, as evidenced also by the analysis of the local entrainment rate
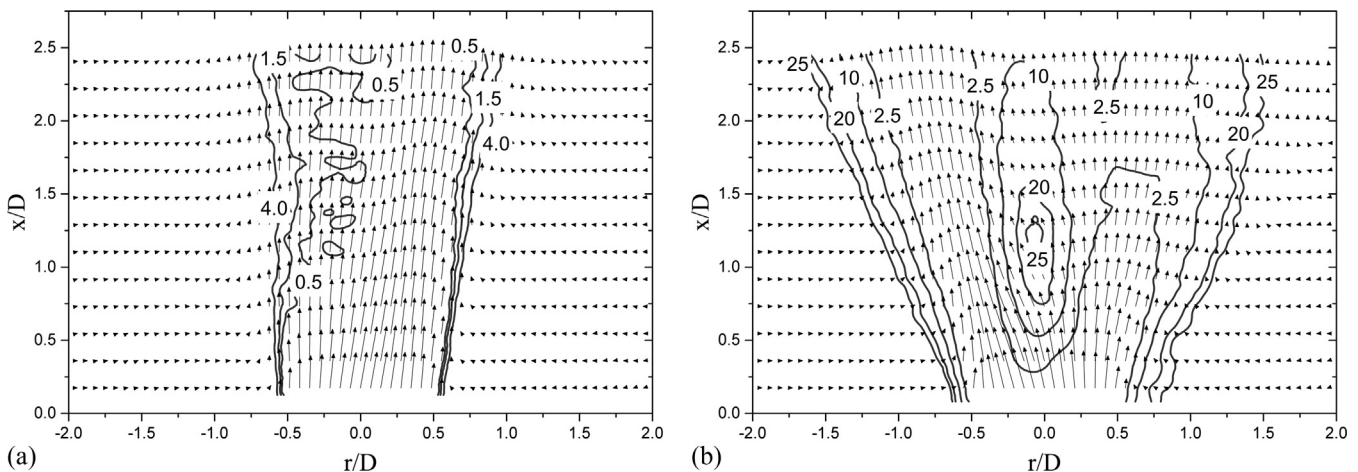

Fig. 8. Time-mean vector fields (vectors represent the in-plane velocity components) for the: (a) $S = 0.45$ and (b) $S = 0.78$ cases. Iso-lines of equal probability are superimposed on the vector field and quoted with the value of p expressed as a percentage.
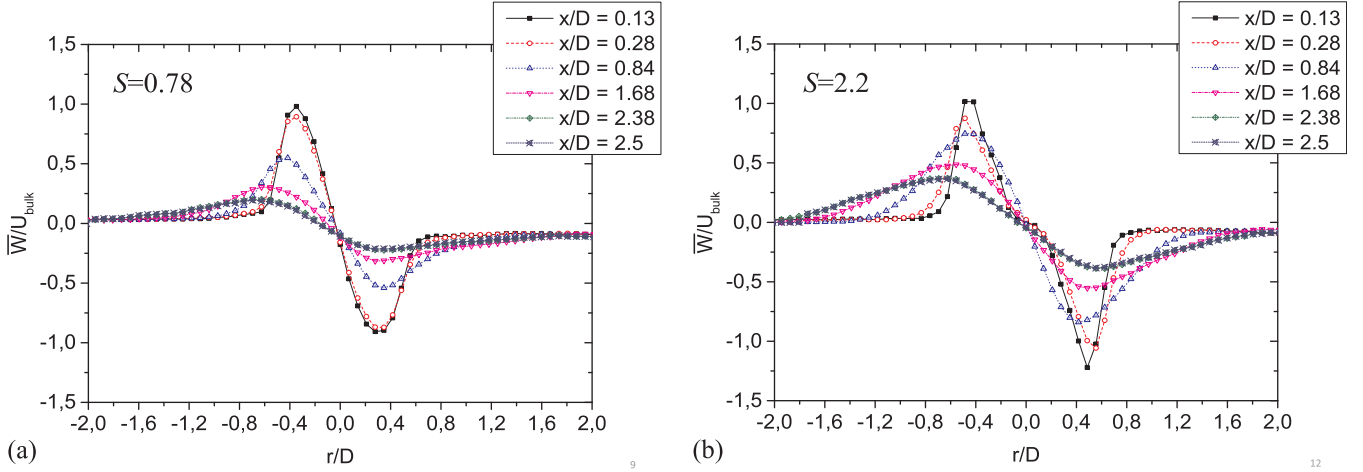
Fig. 9. Radial profiles of the time averaged azimuthal velocity component at increasing axial distance from the nozzle for two swirl numbers: (a) $S = 0.78$; (b) $S = 2.2$.

shown in the next section. On the other side, for $S < 1.1$ the entrainment rate curves, shown in Fig. 12(a), evidence a positive concavity while a negative one is observed for curves at $S > 1.1$

It is worth noting that Chigier and Beer [37] found similar results for a free turbulent swirling jet. Based on their data, the Reynolds number of their jet was estimated to be about 26,700 with a nozzle diameter D = 25.4 mm. For the reader convenience, the Chigier and Beer's data on entrainment rate have been normalized by x/D and reproduced in Fig. 12(b), where S_{CB} is the swirl number reported in their paper. Unfortunately a quantitative comparison with present results is not possible because of differences in the experimental set-up and in the velocity measurement technique. Anyhow the qualitative agreement is very good, their data show higher entrained flow rates at increasing swirl and an almost linear increase along the streamwise coordinate x/D for $S_{CB} = 0.47$ (see Fig. 12b). Our results qualitatively confirm also the main features of those of [39] for a similar Reynolds number (Re = 20,500) and reported in Fig. 12(c), where S_{PS} is the swirl number reported in their paper. It must be considered that the Swirl numbers range investigated in [39] covers a range similar to the one in the present paper, although the precise values may not be comparable, being measured with different techniques and for different nozzles.

The variation of the entrainment rate with swirl number at several locations downstream of the nozzle exit is reported in Fig. 13. The data indicate that in the investigated initial region of the jet $\Psi(x/D)$ increases with swirl at different rates with the distance from the nozzle. A systematic non-linearity is observed for swirl intensities around $S = 0.8$, just below the critical swirl number, which in our jet can be assumed to be $S = 1.1$. This non-linearity may be justified by the abrupt change of the jet structure at the insurgence of vortex breakdown, see Figs. 5 and 6. These results are in general agreement with those reported in [39], where the same trend and a more pronounced enhancement of entrainment was found as S increases beyond the critical swirl number.

It is also interesting to analyze the behaviour of the local entrainment rate K_{el}, which could be estimated directly from the measured non-dimensional entrainment rate, $\Psi(x/D)$, by using Eq. (8). Anyhow the derivative operator in Eq. (8) increases the uncertainty in the estimated value of K_{el} by amplifying noise. Thus a 5 points moving average was applied to the measured values of $\Psi(x/D)$ shown in Fig. 12(a), this removes some of the noise without smoothing too much the curve. Then the filtered data belonging to a streamwise interval of the same size used for the moving average, i.e. about 0.28 D, were fitted to a straight line of equation $\Psi_{fitt}(x/D) = \overline{K}_{el}*(x/D) + q_{fitt}$ by a least square method. The fitting parameter $\overline{K}_{el}$ has been assumed as the mean value of K_{el} over the fitting interval. For the tested cases, the value of $\overline{K}_{el}$ was computed over streamwise intervals centred at x/D = 0.5, 1.0, 1.5, 2.0

and results are shown in Fig. 14. The set of axial positions is chosen as to follow the progressive elongation of the recirculation bubble shown by Fig. 7 at increasing swirl level. The aim is to evidence that while the entrainment rate increases with the swirl number, see Fig. 13, its behaviour along the downstream direction depends on the jet structure forced by the swirl level.

For the non-swirling jet we observe a slight increase of $\overline{K}_{el}$ in the streamwise direction in agreement with the results of Hill [21] and Han and Mungal [32]. For x/D ≥ 2 $\overline{K}_{el}$ stabilizes to about 0.33, very close to the corresponding value of 0.32 found by Hill [21] in the fully developed region of a turbulent non-swirling jet.

With a moderate increase of the swirl, i.e. going from $S = 0$ to $S = 0.45$, the values of $\overline{K}_{el}$ increase, proportionally with the distance from the jet exit, reaching a value of about 0.6 at x/D = 2 almost double than the one found for the non-swirling case. This trend is in qualitative agreement with the results of Chigier and Beer [37], Chigier and Chervinsky [38], Orlu et al. [27] and Park and Shin [39]. It is interesting to observe that in the pre-breakdown regime also the jet width increases proportionally with the distance from the jet exit, see Fig. 5. A further increase of the swirl number in the range $0.78 \leqslant S < 1.1$ forced the jet to the transition regime between the pre- and the post-breakdown conditions. The asymmetric jet structure observed in this regime jeopardizes a reliable analysis of $\overline{K}_{el}$. Once transitioned to the fully developed breakdown regime, i.e. $S \geq 1.1$, the jet at first rapidly enlarges in the radial direction near the nozzle exit, where a central reverse/stagnation axial flow shows up, then its spread progressively reduces moving further downstream, Fig. 5(d–f). In this regime, $\overline{K}_{el}$ increases quickly moving downstream and reaches its maximum value at about x/D = 1.0, while further downstream it progressively decreases. It is worth noting that the central recirculating flow, Fig. 7, and the strongest vortical structures associated to PVC are both located in the region x/D $\lesssim$ 1.5 [19]. Downstream the above region $\overline{K}_{el}$ assumes an almost constant value of about 0.65, for any swirl number above 1, see Fig. 14.

5. Conclusions

The initial region of a swirling gas jet has been investigated experimentally using Stereo Particle Image Velocimetry (SPIV) in order to quantify the entrainment rate as a function of the measured swirl number and axial distance from the nozzle. The experiments were carried out on a model burner used to generate a isothermal gas jet issuing into ambient air at Reynolds number, Re = 21,800, sufficiently high to favour the development of a free turbulent jet and to allow comparison with previously published results with and without swirl. The entrainment rate was evaluated by using the integral method
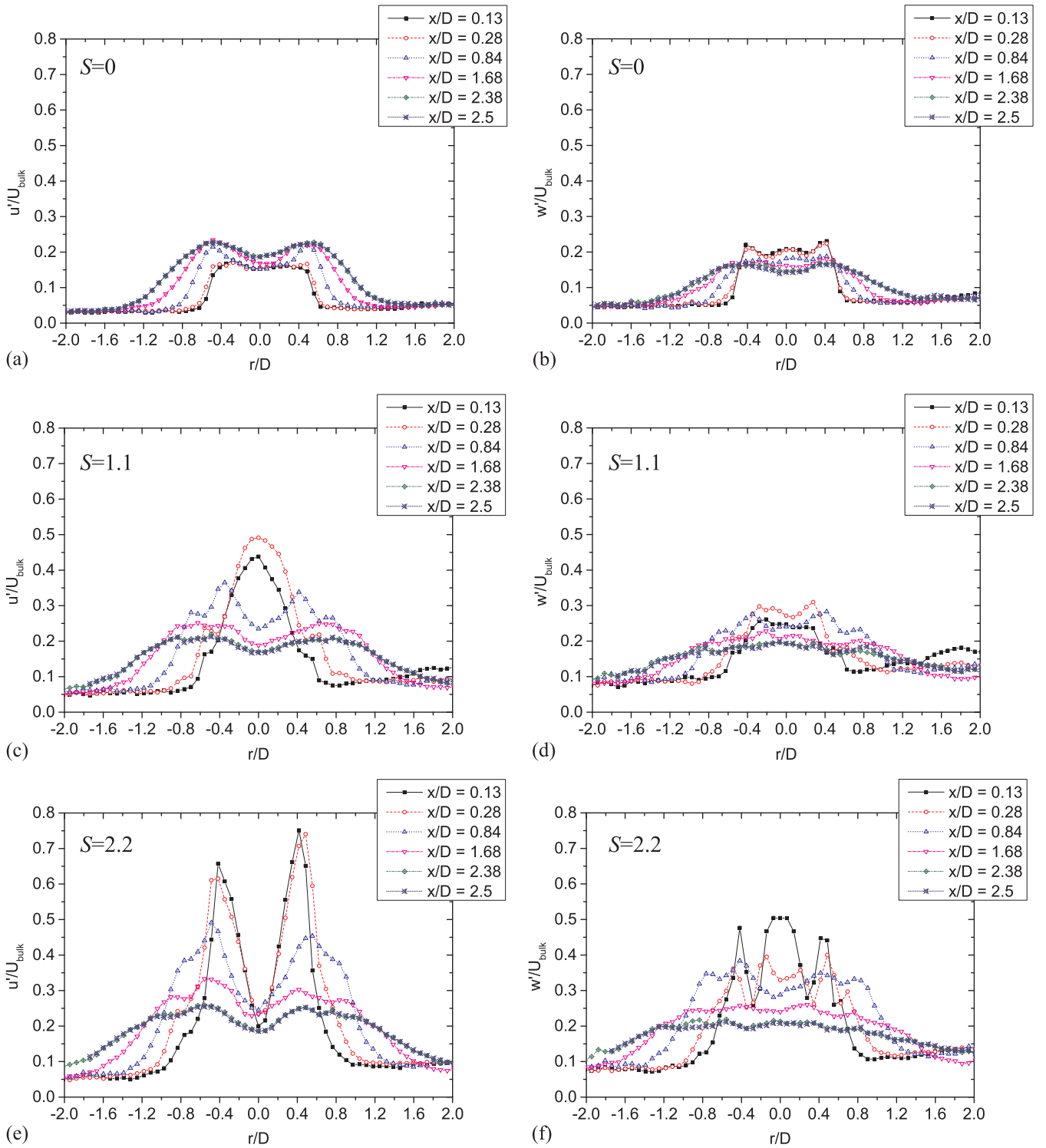
Fig. 10. Radial profiles of the r.m.s. of the axial (a, c, e) and tangential (b, d, f) velocity fluctuations at increasing axial distance from the nozzle and for different swirl numbers S.

applied to the time-averaged SPIV measured velocity maps. The study was also able to identify the presence of vortex breakdown, central recirculation zone (CRZ) and precessing vortex core (PVC). It also revealed asymmetries in the jet structure at moderate swirl, associated with the random in time and asymmetric in space occurrence of a reverse/stagnation flows not detectable in the mean velocity maps. After vortex breakdown, velocity fluctuations become very large in the inner shear layer between the central recirculation region and the jet main stream, indicating the intense mixing favoured by the large scale vortical structures originated by the high swirl.

The results provide quantitative evidence that the entrainment rate in the near field is enhanced considerably by the swirl, especially after the onset of vortex breakdown and PVC, reaching values significantly larger than those measured in non-swirling jets.

Further analysis of the mean local entrainment rate reveals an overall increase of $\overline{K}_{el}$ with the swirl number in the investigated region of the jet. The value of $\overline{K}_{el}$ increases in the pre-breakdown regime also with distance from the nozzle, while in the post-breakdown regime for $x/D > 1$ the opposite is true, and at $x/D > 1.5$ the local entrainment rate assumes an almost constant value of about 0.65, for any swirl
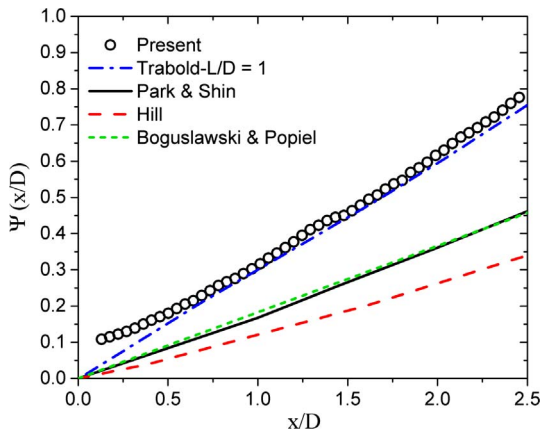
Fig. 11. Normalized entrainment rate, Ψ, vs normalized axial distance from the jet outlet, x/D, in the initial region of a free non-swirling jet. Comparison between literature data and present result.

number above 1. These results evidence that both VB and PVC affect the entrainment process in a complex way, linked to the abrupt change they induce in the flow field structure.

The significance of the present results consists in providing improved understanding of fuel–air mixing in the initial region of a typical
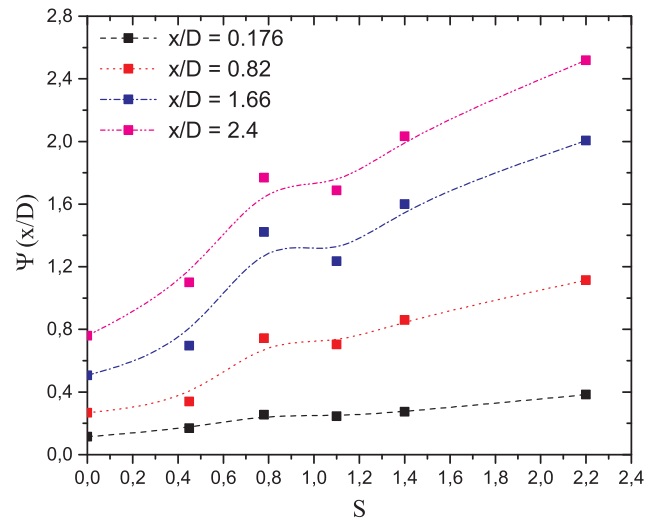
Fig. 13. Entrainment rates, Ψ(x/D), measured at several axial locations as function of swirl number *S*.

burner with swirl, as a function of the swirl number. Moreover, the reported quantitative data have practical relevance to help obtaining performance enhancement and optimization of mixing in the initial
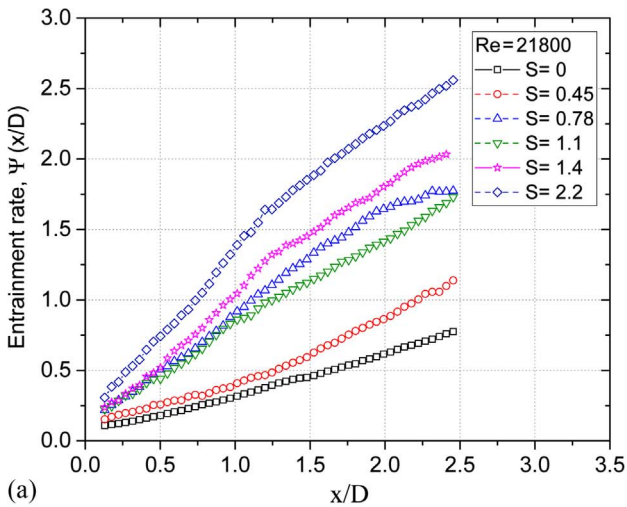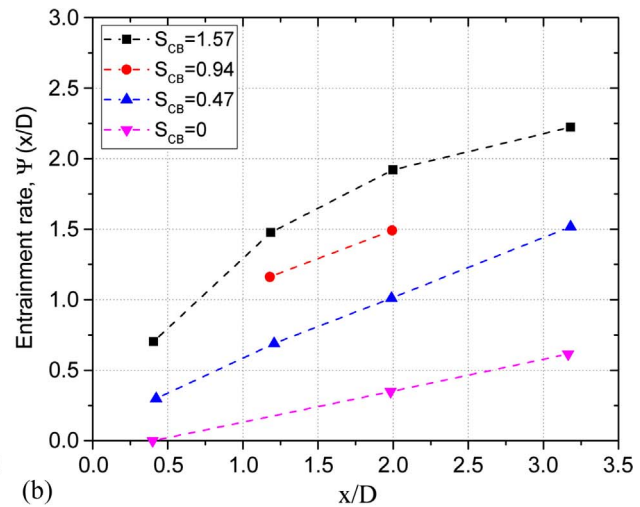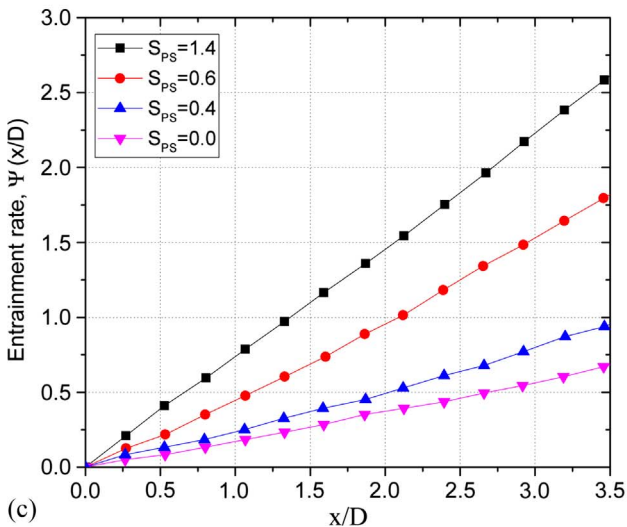
Fig. 12. Entrainment rate, Ψ, vs normalized axial distance from the jet outlet, x/D, at increasing swirl number. Symbols are experimental data, lines are shown just for convenience. (a) Present work. (b) Entrainment rate, Ψ, computed from data of [37]. (c) Entrainment rate data, Ψ, from [39].
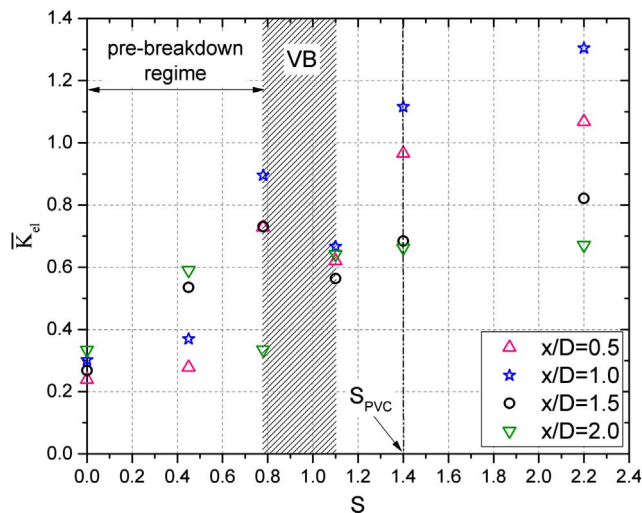
Fig. 14. Average local entrainment rate, $\overline{K}_{el}$ as function of swirl number, S, evaluated at several axial locations. The shaded area represents the transition region between pre-breakdown and post-breakdown flow regime, $S_{PVC} = 1.4$ is the swirl number at which PVC is first observed.

region of a typical burner and may also be useful to validation of numerical modelling of the combustion process.

Acknowledgements

References

[1] T.S. Cheng, Y.-C. Chao, D.-C. Wu, T. Yuan, C.-C. Lu, C.-K. Cheng, J.-M. Chang, Effects of fuel-air mixing on flame structures and NOx emissions in swirling me-thane jet flames, Symp. Combust. 27 (1998) 1229–1237, http://dx.doi.org/10. 1016/S0082-0784(98)80527-4.

[2] G. Solero, A. Coghe, Effect of injection typology on turbulent homogeneous mixing in a natural gas swirl burner, Exp. Therm. Fluid Sci. (2000) 162–170, http://dx.doi.org/10.1016/S0894-1777(99)00067-9.

[3] A. Olivani, G. Solero, F. Cozzi, A. Coghe, Near field flow structure of isothermal swirling flows and reacting non-premixed swirling flames, Exp. Therm. Fluid Sci. 31 (2007) 427–436.

[4] E. Canepa, P. Di Martino, P. Formosa, M. Ubaldi, P. Zunino, Unsteady aerodynamics of an aeroengine double swirler lean premixing prevaporizing burner, J. Eng. Gas Turbines Power 128 (2006) 29, http://dx.doi.org/10.1115/1.1924720.

[5] F. Cozzi, A. Coghe, Effect of air staging on a coaxial swirled natural gas flame, Exp. Therm. Fluid Sci. 43 (2012) 32–39, http://dx.doi.org/10.1016/j.expthermflusci. 2012.04.002.

[6] A.K. Gupta, D.G. Lilley, N. Syred, Swirl Flows, Abacus Press, 1984.

[7] I.K. Toh, D. Honnery, J. Soria, Axial plus tangential entry swirling jet, Exp. Fluids 48 (2010) 309–325, http://dx.doi.org/10.1007/s00348-009-0734-2.

[8] A. Coghe, G. Solero, G. Scribano, Recirculation phenomena in a natural gas swirl combustor, Exp. Therm. Fluid Sci. 28 (2004) 709–714, http://dx.doi.org/10.1016/j.expthermflusci.2003.12.007.

[9] A.K. Gupta, M.J. Lewis, M. Daurer, Swirl effects on combustion characteristics of premixed flames, J. Eng. Gas Turbines Power 123 (2001) 619, http://dx.doi.org/10.1115/1.1339987.

[10] O. Lucca-Negro, T. O'Doherty, Vortex breakdown: a review, Prog. Energy Combust. Sci. 27 (2001) 431–481, http://dx.doi.org/10.1016/S0360-1285(00)00022-8.

[11] K. Oberleithner, C.O. Paschereit, R. Seele, I. Wygnanski, Formation of turbulent vortex breakdown: intermittency criticality, and global instability, AIAA J. 50 (2012) 1437–1452, http://dx.doi.org/10.2514/1.J050642.

[12] C.E. Cala, E.C. Fernandes, M.V. Heitor, S.I. Shtork, Coherent structures in unsteady swirling jet flow, Exp. Fluids 40 (2006) 267–276, http://dx.doi.org/10.1007/s00348-005-0066-9.

[13] F. Martinelli, A. Olivani, A. Coghe, Experimental analysis of the precessing vortex core in a free swirling jet, Exp. Fluids 42 (2007) 827–839, http://dx.doi.org/10.1007/s00348-006-0230-x.

[14] S.I. Shtork, C.E. Cala, E.C. Fernandes, Experimental characterization of rotating

flow field in a model vortex burner, Exp. Therm. Fluid Sci. 31 (2007) 779–788, http://dx.doi.org/10.1016/j.expthermflusci.2006.08.008.

[15] K. Oberleithner, M. Sieber, C.N. Nayeri, C.O. Paschereit, C. Petz, H.-C. Hege, B.R. Noack, I. Wygnanski, Three-dimensional coherent structures in a swirling jet undergoing vortex breakdown: stability analysis and empirical mode construction, J. Fluid Mech. 679 (2011) 383–414, http://dx.doi.org/10.1017/jfm.2011.141.

[16] F. Martinelli, F. Cozzi, A. Coghe, Phase-locked analysis of velocity fluctuations in a turbulent free swirling jet after vortex breakdown, Exp. Fluids (2012) 1–13, http://dx.doi.org/10.1007/s00348-012-1296-2.

[17] K. Oberleithner, C.O. Paschereit, I. Wygnanski, On the impact of swirl on the growth of coherent structures, J. Fluid Mech. 741 (2014) 156–199, http://dx.doi.org/10.1017/jfm.2013.669.

[18] D.M. Markovich, S.S. Abdurakipov, L.M. Chikishev, V.M. Dulin, K. Hanjalić, Comparative analysis of low- and high-swirl confined flames and jets by proper orthogonal and dynamic mode decompositions, Phys. Fluids 26 (2014) 65109, http://dx.doi.org/10.1063/1.4884915.

[19] R. Sharma, F. Cozzi, A. Coghe, Phase-averaged characterization of turbulent iso-thermal free swirling jet after vortex breakdown, in: Proc. 18th Int. Symp. Appl. Laser Imaging Tech. to Fluid Mech., Lisbon, 2016: pp. 3315–3335. http://ltces.dem.ist.utl.pt/lxlaser/lxlaser2016/finalworks2016/papers/02.4_2_233paper.pdf (accessed May 2, 2017).

[20] F.P. Ricou, D.B. Spalding, Measurements of entrainment by axisymmetrical turbulent jets, J. Fluid Mech. 11 (1961) 21, http://dx.doi.org/10.1017/S0022112061000834.

[21] B.J. Hill, Measurement of local entrainment rate in the initial region of axisymmetric turbulent air jets, J. Fluid Mech. 51 (1972) 773, http://dx.doi.org/10.1017/S0022112072001351.

[22] M.A. Delichatsios, L. Orloff, Entrainment measurements in turbulent buoyant jet flames and implications for modeling, Symp. Combust. 20 (1985) 367–375, http://dx.doi.org/10.1016/S0082-0784(85)80523-3.

[23] H.A. Becker, S. Yamazaki, Entrainment, momentum flux and temperature in vertical free turbulent diffusion flames, Combust. Flame 33 (1978) 123–149, http://dx.doi.org/10.1016/0010-2180(78)90055-X.

[24] L. Boguslawski, C.O. Popiel, Flow structure of the free round turbulent jet in the initial region, J. Fluid Mech. 90 (1979) 531, http://dx.doi.org/10.1017/S0022112079002378.

[25] H. Fondse, H. Leijdens, G. Ooms, On the influence of the exit conditions on the entrainment rate in the development region of a free, round, turbulent jet, Appl. Sci. Res. 40 (1983) 355–375, http://dx.doi.org/10.1007/BF00383041.

[26] T.A. Trabold, E.B. Esen, N.T. Obot, Entrainment by Turbulent Jets Issuing from Sharp-Edged Inlet Round Nozzles, J. Fluids Eng. ASME 109 (1987) 248–254, http://dx.doi.org/10.1115/1.3242655.

[27] R. Örlü, P.H. Alfredsson, An experimental study of the near-field mixing characteristics of a swirling jet, Flow Turbul. Combust. 80 (2008) 323–350, http://dx.doi.org/10.1007/s10494-007-9126-y.

[28] G.E. Cossali, A. Coghe, L. Araneo, Near-field entrainment in an impulsively started turbulent gas jet, AIAA J. 39 (2001) 1113–1122, http://dx.doi.org/10.2514/3.14846.

[29] J.-Y. Ha, N. Iida, G.T. Sato, A. Hayashi, H. Tanabe, Experimental investigation of entrainment into diesel spray, SAE Tech. Pap. (1984) 841078, http://dx.doi.org/10.4271/841078.

[30] G.E. Cossali, G. Brunello, A. Coghe, LDV characterization of air entrainment in transient diesel sprays, SAE Tech. Pap. (1991), http://dx.doi.org/10.4271/910178.

[31] B.V. Rajalingam, P.V. Farrell, The Effect of Injection Pressure on Air Entrainment into Transient Diesel Sprays, in: 1999. doi: 10.4271/1999-01-0523.

[32] D. Han, M.G. Mungal, Direct measurement of entrainment in reacting/nonreacting turbulent jets, Combust. Flame 124 (2001) 370–386, http://dx.doi.org/10.1016/S0010-2180(00)00211-X.

[33] D. Liepmann, M. Gharib, The role of streamwise vorticity in the near-field entrainment of round jets, J. Fluid Mech. 245 (1992) 643, http://dx.doi.org/10.1017/S0022112092000612.

[34] A.M. Falcone, J.C. Cataldo, Entrainment velocity in an axisymmetric turbulent jet, J. Fluids Eng. 125 (2003) 620, http://dx.doi.org/10.1115/1.1595674.

[35] M. El Hassan, A. Meslem, Time-resolved stereoscopic particle image velocimetry investigation of the entrainment in the near field of circular and daisy-shaped orifice jets, Phys. Fluids 22 (2010) 35107, http://dx.doi.org/10.1063/1.3358465.

[36] W.G. Rose, A swirling round turbulent jet: 1—mean-flow measurements, J. Appl. Mech. 29 (1962) 615, http://dx.doi.org/10.1115/1.3640644.

[37] N.A. Chigier, J.M. Beér, Velocity and static-pressure distributions in swirling air jets issuing from annular and divergent nozzles, J. Basic Eng. 86 (1964) 788–796, http://dx.doi.org/10.1115/1.3655956.

[38] N.A. Chigier, A. Chervinsky, Experimental investigation of swirling vortex motion in jets, J. Appl. Mech. 34 (1967) 443–451, http://dx.doi.org/10.1115/1.3607703.

[39] S.H. Park, H.D. Shin, Measurements of entrainment characteristics of swirling jets, Int. J. Heat Mass Transf. 36 (1993) 4009–4018, http://dx.doi.org/10.1016/0017-9310(93)90151-U.

[40] S. Wang, Z. Rusak, The dynamics of a swirling flow in a pipe and transition to axisymmetric vortex breakdown, J. Fluid Mech. 340 (1997) 177–223, http://dx.doi.org/10.1017/S0022112097005272.

[41] M. Stöhr, R. Sadanandan, W. Meier, Phase-resolved characterization of vortex–flame interaction in a turbulent swirl flame, Exp. Fluids 51 (2011) 1153–1167, http://dx.doi.org/10.1007/s00348-011-1134-y.

[42] J. Ji, J.P. Gore, Flow structure in lean premixed swirling combustion, Proc. Combust. Inst. 29 (2002) 861–867, http://dx.doi.org/10.1016/S1540-7489(02)80110-9.

[43] A.K. Prasad, Stereoscopic particle image velocimetry, Exp. Fluids 29 (2000)

103–116, http://dx.doi.org/10.1007/s003480000143.

[44] S.M. Soloff, R.J. Adrian, Z.-C. Liu, Distortion compensation for generalized stereo-scopic particle image velocimetry, Meas. Sci. Technol. 8 (1997) 1441–1454, http://dx.doi.org/10.1088/0957-0233/8/12/008.

[45] J. Stafford, E. Walsh, V. Egan, A statistical analysis for time-averaged turbulent and fluctuating flow fields using particle image velocimetry, Flow Meas. Instrum. 26 (2012) 1–9, http://dx.doi.org/10.1016/j.flowmeasinst.2012.04.013.

[46] M. Raffel, C. Willert, J. Kompenhans, Particle Image Velocimetry, second ed., Springer Berlin Heidelberg, Berlin, Heidelberg, 2007, , http://dx.doi.org/10.1007/978-3-540-72308-0.

[47] J. Westerweel, Theoretical analysis of the measurement precision in particle image velocimetry, Exp. Fluids 29 (2000) S003–S012, http://dx.doi.org/10.1007/s003480070002.

[48] S.C. Crow, F.H. Champagne, Orderly structure in jet turbulence, J. Fluid Mech. 48 (1971) 547–591, http://dx.doi.org/10.1017/S0022112071001745.

[49] I. Wygnanski, H.E. Fiedler, The two-dimensional mixing region, J. Fluid Mech. 41 (1970) 327–361, http://dx.doi.org/10.1017/S0022112070000630.

[50] T.C. Claypole, N. Syred, The effect of swirl burner aerodynamics on NOx formation, Symp. Combust. 18 (1981) 81–89, http://dx.doi.org/10.1016/S0082-0784(81)80013-6.

[51] H. Liang, T. Maxworthy, An experimental investigation of swirling jets, J. Fluid Mech. 525 (2005) 115–159, http://dx.doi.org/10.1017/S0022112004002629.

[52] E.C. Fernandes, M.V. Heitor, S.I. Shtork, An analysis of unsteady highly turbulent swirling flow in a model vortex combustor, Exp. Fluids 40 (2006) 177–187, http://dx.doi.org/10.1007/s00348-005-0034-4.

[53] M. Legrand, J. Nogueira, A. Lecuona, S. Nauri, P.A. Rodríguez, Atmospheric low swirl burner flow characterization with stereo PIV, Exp. Fluids 48 (2010) 901–913, http://dx.doi.org/10.1007/s00348-009-0775-6.

[54] N. Syred, A review of oscillation mechanisms and the role of the precessing vortex core (PVC) in swirl combustion systems, Prog. Energy Combust. Sci. 32 (2006) 93–161, http://dx.doi.org/10.1016/j.pecs.2005.10.002.